國立臺灣大學電機資訊學院資訊工程學系暨研究所

碩士論文

Department of Computer Science and Information Engineering

College of Electrical Engineering and Computer Science

National Taiwan University

Master's Thesis

# 透過分佈差異和特徵異質性進行主動 3D 物體偵測

# Distribution Discrepancy and Feature Heterogeneity for Active 3D Object Detection

陳皇宇

Huang-Yu Chen

指導教授: 徐宏民 博士

Advisor: Winston H. Hsu Ph.D.

中華民國 113 年 6 月

June, 2024

doi:10.6342/NTU202401627

# 國立臺灣大學碩士學位論文
# 口試委員會審定書
## MASTER'S THESIS ACCEPTANCE CERTIFICATE
## NATIONAL TAIWAN UNIVERSITY

# 透過分佈差異和特徵異質性進行主動 3D 物體偵測

# Distribution Discrepancy and Feature Heterogeneity for Active 3D Object Detection

本論文係陳皇宇君(學號R11922A06)在國立臺灣大學資訊工程學系人工智慧碩士班完成之碩士學位論文, 於民國113年6月28日承下列考試委員審查通過及口試及格, 特此證明。

The undersigned, appointed by the Master Program of Artificial Intelligence offered by the Department of Computer Science and Information Engineering on 28 June 2024 have examined a Master's thesis entitled above presented by CHEN, HUANG-YU (student ID: R11922A06) candidate and hereby certify that it is worthy of acceptance.

口試委員Oral examination committee:

| | | |
|---|---|---|
| (指導教授Advisor) | 陳文進 | 葉梅珍 |
| | | |
| | | |

系(所)主管Director: 陳祝嵩



doi:10.6342/NTU202401627

# 摘要

基於光學雷達的 3D 物體檢測是自動駕駛和機器人發展的關鍵技術。然而，資料標註的成本過高限制了其發展。我們提出一種新穎且有效的主動學習方法，名為分布差異與特徵異質性（DDFH），該方法同時考慮幾何特徵和模型嵌入，從實例層面和框架層面評估信息。分布差異評估未標記和已標記分布中實例的差異性和新穎性，使模型能夠在有限的數據下高效學習。特徵異質性確保框架內實例特徵的異質性，保持特徵多樣性，同時避免冗餘或相似實例，從而最小化標註成本。最後，使用分位數變換有效地聚合多個指標，提供一個統一的資訊量指標。廣泛的實驗表明，DDFH 在 KITTI 和 Waymo 數據集上超越了當前最先進（SOTA）方法，有效地減少了標定框標註成本 56.3，並在單階段和雙階段的模型中展現出穩健性。

**關鍵字：**主動學習、光學雷達 3D 物件偵測、自動駕駛



doi:10.6342/NTU202401627



doi:10.6342/NTU202401627

# Abstract

LiDAR-based 3D object detection is a critical technology for the development of autonomous driving and robotics. However, the high cost of data annotation limits its advancement. We propose a novel and effective active learning (AL) method called Distribution Discrepancy and Feature Heterogeneity (DDFH), which simultaneously considers geometric features and model embeddings, assessing information from both the instance-level and frame-level perspectives. Distribution Discrepancy evaluates the difference and novelty of instances within the unlabeled and labeled distributions, enabling the model to learn efficiently with limited data. Feature Heterogeneity ensures the heterogeneity of intra-frame instance features, maintaining feature diversity while avoiding redundant or similar instances, thus minimizing annotation costs. Finally, multiple indicators are efficiently aggregated using Quantile Transform, providing a unified measure of informativeness. Extensive experiments demonstrate that DDFH outperforms the current state-of-the-art (SOTA) methods on the KITTI and Waymo datasets, effectively reducing the



doi:10.6342/NTU202401627

bounding box annotation cost by 56.3% and showing robustness when working with both one-stage and two-stage models.

**Keywords:** Active Learning, LiDAR 3D Object Detection, Autonomous Driving



doi:10.6342/NTU202401627

# Contents





doi:10.6342/NTU202401627

doi:10.6342/NTU202401627

# List of Figures





doi:10.6342/NTU202401627

doi:10.6342/NTU202401627

# List of Tables





doi:10.6342/NTU202401627



doi:10.6342/NTU202401627

# Chapter 1 Introduction

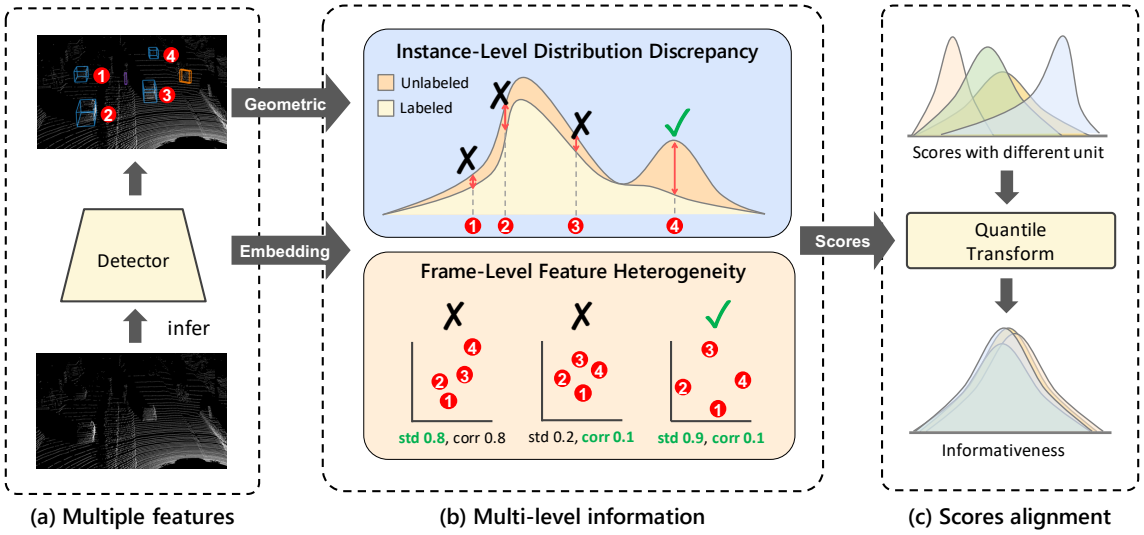


Figure 1.1: The three core concepts of DDFH. (a) Embedding and geometric features are used as DDFH inputs. (b) Considering instance-level distribution discrepancy and frame-level feature heterogeneity ensures that instances remain highly informative across all levels. (c) After transforming various indicators using the Quantile Transform, it effectively aggregates to estimate the final informativeness.

Research on LiDAR-based 3D object detection [4, 26] has emerged due to its significant potential and applications. However, annotating LiDAR data requires locating multiple objects in three-dimensional space, which is expensive and time-consuming. Therefore, obtaining annotated data more efficiently within limited time and resources has become a crucial and unavoidable issue. Several studies have attempted to reduce annotation costs through Auto Labeling [12, 44] or Domain Adaptation [36, 38], which rely on a small number of annotated samples. However, unstable annotation accuracy and restricted domain shifts may limit their usage in various applications.


doi:10.6342/NTU202401627

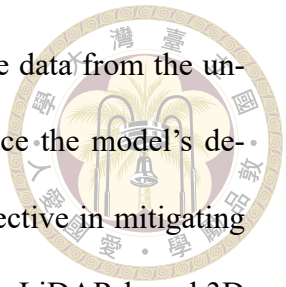

Active Learning (AL) focuses on choosing the most informative data from the unlabeled pool for human annotation, is a significant solution to reduce the model's dependence on the amount of data. Although AL has been proven effective in mitigating annotation costs in various research domains [8, 20], its application to LiDAR-based 3D Object Detection is underexplored, with three main challenges remaining unresolved: (1) Compared to 2D object detection, LiDAR-based object detection has additional geometric features (such as rotation and point density) that need to be considered. (2) While the detector's predictions are instance-level, the selection in AL is frame-level, making it challenging to propagate from instances to frames and estimate informativeness. (3) Aggregating multiple indicators under different units and scales is also challenging.

Previous work has used general AL strategies such as entropy and ensemble methods to estimate uncertainty. However, they neglected the unique geometric features in LiDAR-based object detection (first challenge), and solely assessing the instance-level informativeness is insufficient to address the second challenge. A recent work, CRB [17], proposed three heuristic methods to estimate label balance, representativeness, and point density balance through a staged filtering approach. Unfortunately, the filtering order significantly affects sampling results, impacting the fairness among indicators and failing to solve the third challenge. Another work, KECOR [16], proposed a kernel coding rate maximization strategy. However, it also did not consider geometric features and used different weighted settings to aggregate multiple indicators in different datasets, affecting generalization.

To address the above challenges, we propose the Distribution Discrepancy and Feature Heterogeneity (DDFH) method, as illustrated in Fig.1.1, where components (a), (b), and (c) are designed for the first, second, and third challenges, respectively. DDFH lever-


doi:10.6342/NTU202401627

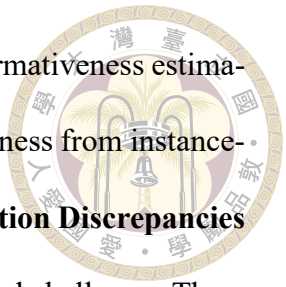

ages model embedding and geometric information as features for informativeness estimation to address the first challenge. Moreover, we explores informativeness from instance-level and frame-level perspectives by considering intra-class **Distribution Discrepancies** (DD) and intra-frame **Feature Heterogeneity** (FH) to tackle the second challenge. Then, DDFH employs a **Quantile Transform** (QT) to normalize each indicator to the same scale, effectively aggregating the indicators to solve the third challenge. Finally, we propose **Confidence Balance** (CB) to evaluate the allocation of annotation resources. Unlike previous methods that solely count selected instances for each category, CB considers the summation of confidence levels for each instance within the same category.

We verify the effectiveness of DDFH through experiments on real-world datasets, KITTI and Waymo Open Dataset. The results indicate that our DDFH method outperforms the existing SOTA, effectively reducing the data annotation cost by 56.3% and achieving an average improvement of 1.8% in 3D mAP with the same amount of data. From our extensive ablation studies, DDFH also demonstrates its generalization when used with both one-stage and two-stage detection models.


doi:10.6342/NTU202401627



doi:10.6342/NTU202401627

# Chapter 2 Related Work

## 2.1 LiDAR-based 3D Object Detection.

LiDAR-based 3D object detection techniques are primarily divided into two categories: point cloud direct processing and voxelization. Methods such as the PointNet series [24, 25] operate directly on point clouds, preserving the original spatial accuracy of the data but are less efficient in handling large-scale data. Recent research, like PointAugmenting [40], introduces cross-modal augmentation, enhancing LiDAR point clouds with deep features extracted from pre-trained 2D object detection models, thereby improving 3D object detection performance. Voxelization methods, such as VoxNet [19] and SECOND [43], convert point clouds into voxel grids to enable efficient 3D convolution, significantly increasing computational speed. The Voxel Transformer (VoTr) [18] architecture effectively expands the model's receptive field, enhancing the ability to capture large-scale environmental information. The PV-RCNN series [32, 33] improves detection accuracy and processing efficiency by fusing point cloud and voxel features. These detectors rely heavily on large volumes of high-quality training data; however, the labeling cost for LiDAR data is quite expensive.


doi:10.6342/NTU202401627

## 2.2 Active learning for object detection.

Active learning selects the most informative samples for annotation, thus mitigating the model's dependence on the volume of data. Numerous general active learning strategies currently exist, such as those based on model uncertainty [5, 10, 12, 23, 34], diversity [1, 6, 30], or hybrid methods that combine both approaches [45]. Estimating in the gradient space is also a common approach (e.g., BADGE [14], BAIT [2]). Research applying these methods to object detection [21, 28, 42, 47] remains limited. Many studies directly use general strategies like maximum entropy [27], bayesian inference [13] to estimate uncertainty in both bounding box and category. LT/C [15] introduces noise-perturbed samples and assesses tightness and stability based on the model' s output. Estimating informativeness through the distribution of embeddings and predictions [7, 22]. Research on LiDAR-based object detection is even scarcer, mainly due to the high computational cost of point cloud processing and the higher dimensionality of regression information. General AL methods (Shannon Entropy [9], ensemble [28]) do not consider geometric features and therefore are not well-suited for LiDAR. Recent work, such as CRB [17], proposes three heuristic methods to incrementally filter samples. KECOR [16] identifies the most informative samples through the lens of information theory. However, these studies fail to effectively integrate multi-level information and do not consider the distribution of selected samples, leading to redundant annotation costs. Therefore, we propose DDFH, which estimates the informativeness based on the distributional differences of instances and intra-frame feature heterogeneity, and effectively aggregates multiple indicators using the quantile transform to estimate multi-level informativeness.


doi:10.6342/NTU202401627

# Chapter 3 Methodology

## 3.1 Active Learning Setup

In the active object detection setup, the labeled set $D^L = \{(P^L, Y^L)\}$ contains a small amount of point clouds $P^L$ with annotations $Y^L$, and $D_U = \{P_U\}$ represents a large unlabeled set of raw point clouds $P_U$. Initially, samples are randomly selected to form $D_L$, and the detection model learns over multiple rounds $r \in \{1, ..., R\}$. The objective of active learning is to evaluate the informativeness of $P_U$ in each round and select the most informative samples to form a new subset $D_s^*$ for human annotation. Then, the $D_s^*$ is merged into $D_L$ to start a new round to retrain the model. This process repeats until the size of the labeled set reaches the annotation budget.

## 3.2 Framework Overview

We propose a novel active learning framework, Distribution Discrepancy and Feature Heterogeneity (DDFH) for LiDAR-based 3D object detection. As illustrated in Fig. 3.1, we infer point clouds $P \in \{D_U, D_L\}$ into the model and get model output containing embeddings and bounding boxes. However, estimating distributions in high-dimensional space is challenging, so we use t-SNE[39] to project embeddings into lower dimensions


doi:10.6342/NTU202401627

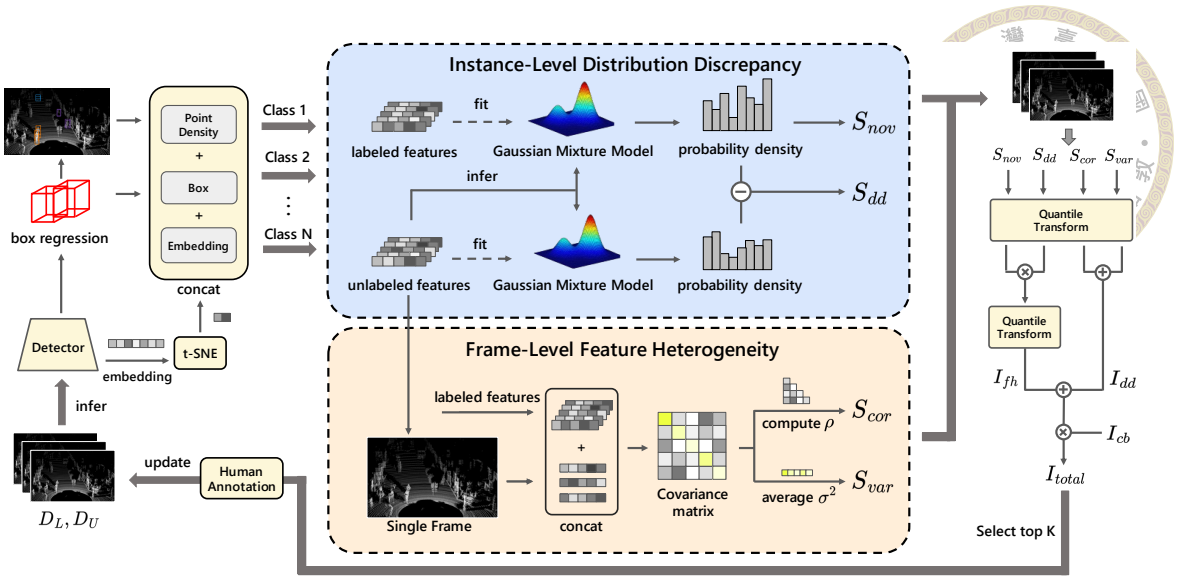


Figure 3.1: DDFH framework for LiDAR-based 3D active object detection. According to the batch active learning[31] setup, one cycle represents a single sampling. DDFH utilizes a Quantile Transform to normalize all metrics before aggregation to estimate informativenes, and then updates the dataset before starting a new round.

while retaining important information, denoted as $\mathbf{f}^{e*} \in \mathbb{R}^2$. The geometric features of LiDAR-based object detection (length, width, height, volume, rotation, and point cloud density) $\mathbf{f}^{g} \in \mathbb{R}^6$ are also significant, as they convey direct information about objects such as occlusion, behavior, and morphology. So we use $\mathbf{f} = [\mathbf{f}^{e*\top}\ \mathbf{f}^{g\top}]^\top \in \mathbb{R}^8$ as the input feature for DDFH, calculating multiple indicators to estimate informativeness. However, since the units of the indicators differ, normalization is required before aggregation.

### 3.2.1 Score Normalization.

DDFH evaluates informativeness based on multiple indicators, but their scales differ, making direct aggregation impossible. Thus, we use Quantile Transform $\psi$ to normalize. $\psi(.,.)$ is a non-linear transform that converts the first input to follow a normal distribution and returns the transformed result of the second input. $\psi$ spreads out the most frequent values and reduces the impact of outliers. Since active learning aimS to select the top k samples, the relative distance of scores is not particularly important. Instead, maintaining


doi:10.6342/NTU202401627

the ranks of various indicators and reducing outliers aids in aggregating the indicators, making $\psi$ a crucial bridge in computing $I_{total}$. Next, we will introduce the operating principles of DDFH sequentially.

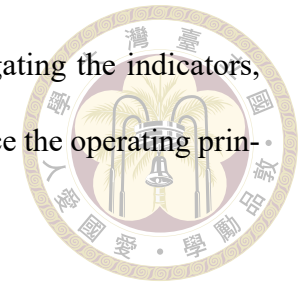

## 3.3 Instance-Level Distribution Discrepancy

Since labeled set is much smaller than the unlabeled set, estimating the distribution is particularly important. Reducing the distribution gap between the labeled set and the unlabeled set will assist the model in inference. Inspired by [22], we use a Gaussian Mixture Model(GMM) to estimate probability density. Unlike previous works, we consider both geometric features and embeddings, using dimensionality reduction to avoid overly sparse space. Intuitively, if an instance appears frequently in the unlabeled set but is rare in the labeled set, such an instance can help the model efficiently understand unlabeled samples. Therefore, for each class $c \in C$, we establish $G_c^L$ fit on $\{\mathbf{f_{c,1}}...\mathbf{f_{c,N_c^L}}\}$ and $G_c^U$ fit on $\{\mathbf{f_{c,1}}...\mathbf{f_{c,N_c^U}}\}$, where $G_c^U$ is a GMM fit on unlabeled features, and $N_c^U$ is the number of instances with class c in the unlabeled set. We estimate the probability density function of each instance in the unlabeled and labeled sets, and calculate the discrepancy score $s_i^{dd}$:

$$s_{c,i}^{dd} = \mathbb{P}_{G_c^U}(\mathbf{f}_{c,i}) - \mathbb{P}_{G_c^L}(\mathbf{f}_{c,i}), \quad i = 1, 2, ..., N_c^U, \tag{3.1}$$

where $\mathbb{P}_{G_c^U}(\mathbf{f}_{i,c})$ represents the probability density of $\mathbf{f}_{i,c}$ in the unlabeled set. However, considering $S_{dd}$ alone is insufficient, as very dense instances might overly influence the indicator, leading to frequent selection of dense but repetitive instances in the early stages. Hence, unlike previous works [7], we also extract $\mathbb{P}_{G_c^L}(\mathbf{f}_{i,c})$ to calculate the novelty score


doi:10.6342/NTU202401627

$s^{nov}$:

$$s_{c,i}^{nov} = -\mathbb{P}_{G_c^L}(\mathbf{f}_{c,i}), \quad i = 1, 2, ..., N_c^U. \tag{3.2}$$

$s^{nov}$ ensures the novelty of instances. If an instance has a high probability density in the labeled set, it indicates that the instance has already been selected, thus the $s^{nov}$ score will decrease, effectively reducing redundant annotation costs. Following these two indicators, $I_{dd}(P_j)$ can be calculated as:

$$I_{dd}(P_j) = \frac{1}{N}\sum_{i=1}^{N}[\psi(S^{dd}, s_i^{dd}) + \psi(S^{nov}, s_i^{nov})], \tag{3.3}$$

where $N$ is the number of instances in $P_j$. $S^{dd}$ is the set of all instances' $s^{dd}$. Ablation studies show that $I_{dd}$ enables the active learning model to learn rapidly with a small amount of data. However, $I_{dd}$ does not consider frame-level information, which may overlook similar instances within the same frame. Therefore, we introduce a second component to address this issue.

## 3.4 Frame-Level Feature Heterogeneity

Object detection is a multiple-instance problem. Considering only instance-level information can lead to redundant annotations. Complex scenes usually contain numerous objects that share the same lighting and environmental factors, making their features highly similar or following linear variations. Such samples are costly to annotate but offer limited assistance to the model. Therefore, we propose frame-level Feature Heterogeneity (FH). As shown in Fig. 1.1b, we decompose heterogeneity into correlation and variance. Denote $F_{j,c}^U = [\mathbf{f}_{j,c,1}^U ... \mathbf{f}_{j,c,m}^U]$ as the feature vector of all instances with class c in j-frame, where $m$ represents the number of instances. FH ensures $F_{j,c}$ can maximize the feature


doi:10.6342/NTU202401627

heterogeneity of the labeled instance vector $F_c^L$. Specifically, we combine the two into $\tilde{F}_{j,c} = [F_{j,c}^U \, F_c^L] \in \mathbb{R}^{8\times N}$ and use covariance $cov$ and variance $\sigma^2$ to calculate the Pearson correlation $\rho$, ensuring non-linear variations among features. The correlation $\rho$ is calculated as:

$$\rho(\hat{F}_{j,c}) = \frac{2}{N_f(N_f-1)} \sum_{k<\ell}^{N_f} \frac{cov(\hat{F}_{j,c}^k, \hat{F}_{j,c}^\ell)}{\sigma(\hat{F}_{j,c}^k) \cdot \sigma(\hat{F}_{j,c}^\ell)}, \tag{3.4}$$

where $\tilde{F}_{j,c}^k$ and $\tilde{F}_{j,c}^\ell$ represent the $k$-th and $\ell$-th feature dimension of matrix $\tilde{F}_{j,c}$, and $\overline{\tilde{F}_{j,c}^k}$ is the mean of $\tilde{F}_{j,c}^k$. $\sigma^2(\tilde{F}_{j,c}^k) = \frac{1}{N}\|\tilde{F}_{j,c}^k - \overline{\tilde{F}_{j,c}^k}\|_2^2$, $N_f$ is the number of feature dimensions of matrix $\tilde{F}_{j,c}$. The smaller the value of $\rho$, the less linear the correlation, enabling the model to learn more feature combinations. However, as shown in Fig. 1.1, considering only correlation overlooks the information about the distance between features. Thus, we also consider $\sigma^2$ to ensure sufficient variation among features. Based on these two indicators, we calculate $s^{cor}$ and $s^{var}$:

$$s_{j,c}^{var} = \sum_{k=1}^{N_f} \sigma^2(\tilde{F}_{j,c}^k), \quad s_{j,c}^{cor} = 1 - |\rho(\tilde{F}_{j,c})|. \tag{3.5}$$

The closer $\rho$ is to 0, the less linear the correlation between features. Conversely, values far from 0 indicate positive or negative correlations. Therefore, we take the absolute value of correlation and subtract it from 1, making the $s_{j,c}^{cor}$ indicator larger. Based on these two scores, we calculate the feature heterogeneity informativeness $I_{fh}(P_j)$ for $P_j$:

$$I_{fh}(P_j) = \frac{1}{C} \sum_{c=1}^{C} \psi(S_{var}, s_{j,c}^{var}) \cdot \psi(S_{cor}, s_{j,c}^{cor}) \tag{3.6}$$

where $S^{var}$ is the set of all $s^{dd}$. $I_{fh}$ ensures instances maintain low correlation and high variance, calculated through multiplication. This introduces the core components of the DDFH approach, exploring informativeness from both instance-level and frame-level per-


doi:10.6342/NTU202401627

spectives.

## 3.5 Confidence Balance for Imbalanced Data

Balancing annotation costs across classes has always been crucial in active learning. Previous works [16, 17] calculate entropy by the number of all categories and the classification logit from the classifier, termed Label Balance (LB). However, these method is limited in imbalanced datasets, as imbalanced classes usually have lower confidence, resulting in more false-positive instances. The actual quantity is often less than expected. Therefore, we propose Confidence Balance (CB) $I_{cb}$, replacing instance quantities with the sum of confidences in each category to better reflect the true class distribution in the frame, enhancing the number of minority classes. $I_{cb}$ can be calculated as follows:

$$I_{cb}(P_j) = -\sum_{c=1}^{C} \phi(p_{j,c}) \ \log \phi(p_{j,c}), \quad \phi(p_{j,c}) = \frac{e^{p_{j,c}}}{\sum_{c=1}^{C} e^{p_{j,c}}}, \tag{3.7}$$

where $p_{j,c}$ represents the sum of confidences of all instances of class c in the j-th frame. We compare the effectiveness of LB and CB sampling in Fig. B.1(c-d), demonstrating the importance of $I_{cb}$ for imbalanced data.



doi:10.6342/NTU202401627

Table 3.1: Compare 3D mAP(%) scores for various AL strategies in the KITTI Dataset with the two-stage 3D detector PV-RCNN

| | | AVERAGE | | | CAR | | | PEDESTRIAN | | | CYCLIST | | |
|---|---|---|---|---|---|---|---|---|---|---|---|---|---|
| | Method | Easy | Mod. | Hard | Easy | Mod. | Hard | Easy | Mod. | Hard | Easy | Mod. | Hard |
| Generic | CORESET [30] | 72.26 | 59.81 | 55.59 | 87.77 | 77.73 | 72.95 | 47.27 | 41.97 | 38.19 | 81.73 | 59.72 | 55.64 |
| | BADGE [3] | 75.34 | 61.44 | 56.55 | 89.96 | 75.78 | 70.54 | 51.94 | 40.98 | 45.97 | 84.11 | 62.29 | 58.12 |
| | LLAL [46] | 73.94 | 62.95 | 58.88 | 89.95 | 78.65 | 75.32 | 46.94 | 45.97 | 45.97 | 75.55 | 60.35 | 55.36 |
| AL Detection | LT/c [15] | 75.88 | 63.23 | 58.89 | 88.73 | 78.12 | 74.87 | 55.17 | 48.37 | 43.63 | 83.72 | 63.21 | 59.16 |
| | Mc-REG [17] | 66.21 | 54.41 | 51.70 | 88.85 | 76.21 | 73.87 | 35.82 | 31.81 | 29.79 | 73.98 | 55.23 | 51.85 |
| | Mc-MI [9] | 71.19 | 57.77 | 53.81 | 86.28 | 75.58 | 71.56 | 41.05 | 37.50 | 33.83 | 86.26 | 60.22 | 56.04 |
| | CONSENSUS [28] | 75.01 | 61.09 | 57.60 | 90.14 | 78.01 | 74.28 | 56.43 | 49.50 | 44.80 | 78.46 | 55.77 | 53.73 |
| | CRB [17] | 79.06 | 66.49 | 61.76 | 90.81 | 79.06 | 74.73 | 62.09 | 54.56 | 48.89 | 84.28 | 65.85 | 61.66 |
| | CRB(offi.) | 80.70 | 67.81 | 62.81 | 90.98 | 79.02 | 74.04 | 64.17 | 50.82 | 50.82 | 86.96 | 67.45 | 63.56 |
| | KECOR [16] | 79.81 | 67.83 | 62.52 | 91.43 | 79.63 | 74.41 | 63.49 | 56.31 | 50.20 | 84.51 | 67.54 | 62.96 |
| | KECOR(offi.) | 81.63 | 68.67 | 63.42 | 91.71 | 79.56 | 74.05 | 65.37 | 57.33 | 51.56 | 87.80 | 69.13 | 64.65 |
| | DDFH(Ours) | **82.27** | **69.84** | **64.76** | **91.76** | **80.65** | **76.46** | **66.37** | **59.40** | **52.97** | **88.68** | **69.47** | **64.85** |

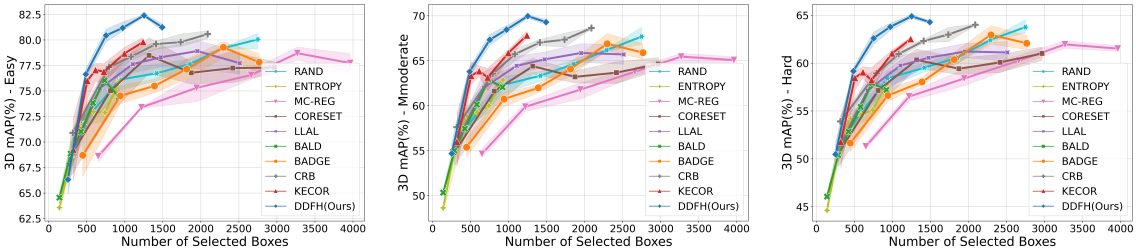


Figure 3.2: 3D mAP(%) of DDFH and AL baseline methods on the KITTI validation split with two-stage model PV-RCNN.

## 3.6 Acquisition Function

As described in 3.2, DDFH combines multiple indicators to explore informativeness comprehensively. Through QT, all indicators are normalized to compute a unified informativeness indicator $I_{total}$, ensuring that the top-k frames are efficient, novel, heterogeneous, and balanced, identifying the optimal selected sets $D_s^*$, formulated as:

$$D_s^* = \underset{D_s \subset D_U}{\arg\max} \quad I_{total}(P_U),\ I_{total}(P_j) = (I_{dd}(P_j) + I_{fh}(P_j)) \cdot I_{cb}(P_j). \tag{3.8}$$

$I_{dd}$ and $I_{fh}$ evaluate informativeness, and multiplying by $I_{cb}$ ensures balanced annotation costs across classes while considering informativeness.



doi:10.6342/NTU202401627



doi:10.6342/NTU202401627

# Chapter 4 Experiment

## 4.1 Experimental Settings

### 4.1.1 3D Point Cloud Datasets.

We tested our method on two real-world datasets: KITTI [11] and Waymo Open Dataset [37]. KITTI contains approximately 7,481 training point clouds (3712 for training, 3769 for validation) with annotations. Each point cloud is annotated with 3D bounding boxes for cars, pedestrians, and cyclists, totaling 80,256 objects. The Waymo Open Dataset provides a large-scale collection of data, it contains 158,361 training point clouds and 40,077 testing point clouds. The sampling intervals for KITTI and Waymo are set to 1 and 10, respectively.

### 4.1.2 Baselines.

We comprehensively evaluated 6 general active learning (AL) methods and 6 AL methods for object detection. RAND selects samples randomly. ENTROPY [41] and LLAL [46] are uncertainty-based methods. CORESET [30] is a diversity-based method. BAIT [2] and BADGE [3] are hybrid methods. MC-MI [9] and MC-REG [17] utilize Bayesian inference. CONSENSUS [28] employs an ensemble to calculate the consensus


doi:10.6342/NTU202401627

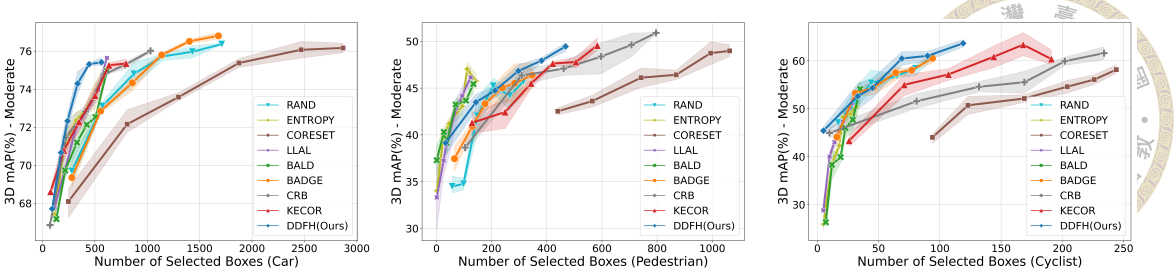


Figure 4.1: 3D mAP(%) of DDFH and the AL Baseline across various categories on the KITTI dataset at the moderate difficulty with SECOND.

score. LT/C evaluates instability and localization tightness. CRB [17] progressively filters based on three heuristic methods. KECOR [16] identifies the most informative sample through the lens of information theory.

### 4.1.3 Evaluation Metrics.

We follow the work of KECOR [16]: In the KITTI dataset, we utilize Average Precision (AP) to evaluate object location in Bird Eye View and 3D, calculated with 40 recall positions. The task difficulty is categorized as EASY, MODERATE (MOD.), and HARD based on the visibility, size, and occlusion/ truncation of the objects. In Waymo, we use Average Precision with Heading (APH), which incorporates both bounding box overlap and orientation accuracy. It categorizes objects into Level 1 (at least five LiDAR points, easier to detect) and Level 2 (all objects, including more challenging scenarios).

### 4.1.4 Implementation Details.

We strive to avoid excessive parameter tuning by using a unified set of hyper-parameters across all experiments. We set the perplexity for t-SNE to 100. For Gaussian Mixture Model, set number of components to 10, reg_covar to 1e-2 to increase generalization and initialize parameters by k-means++.


doi:10.6342/NTU202401627

Table 4.1: Compare 3D mAP and BEV scores for general AL and AL for detection in KITTI Dataset with SECOND

| | | 3D Detection mAP | | | BEV Detection mAP | | |
|---|---|---|---|---|---|---|---|
| Method | Venue | EASY | MOD. | HARD | EASY | MOD. | HARD |
| RAND | | 66.67 | 53.15 | 49.12 | 72.65 | 60.94 | 57.12 |
| ENTROPY [41] | IJCNN'14 | 69.29 | 56.58 | 51.59 | 74.52 | 63.38 | 58.65 |
| BALD [10] | ICML'17 | 68.78 | 55.49 | 50.30 | 74.21 | 62.51 | 57.70 |
| CORESET [30] | ICLR'18 | 65.96 | 51.79 | 47.65 | 73.85 | 60.22 | 56.06 |
| LLAL [46] | CVPR'19 | 68.51 | 56.05 | 50.97 | 74.57 | 63.64 | 58.92 |
| BADGE [3] | ICLR'20 | 69.09 | 55.20 | 50.72 | 75.12 | 63.05 | 58.81 |
| BAIT [2] | NeurIPS'21 | 69.45 | 55.61 | 51.25 | 76.04 | 63.49 | 53.40 |
| CRB [17] | ICLR'23 | 71.69 | 57.16 | 52.35 | 78.01 | 64.71 | 60.04 |
| KECOR [16] | ICCV'23 | 71.85 | 57.75 | 52.56 | 78.30 | 65.41 | 60.15 |
| DDFH(Ours) | | **74.13** | **60.61** | **55.48** | **79.65** | **67.95** | **63.10** |

## 4.2 Main Results

Since the most of baseline method do not provide initial selection samples, to present the results more fairly, we reproduce most of the baseline methods using the same initial settings and provided the official reported performance of two recent methods (CRB and KECOR) in our experiments.

### 4.2.1 DDFH with Two-Stage Detection Model.

For the KITTI dataset, We ran each method three times. As show in Fig. 3.2, our method outperforms all baseline methods. Compared with the CRB and KECOR, the annotation cost is reduced by 51.7% and 33.2%, respectively, especially when the number of annotations is small, the growth rate is particularly fast. In Table 3.1, we follow the KECOR setting, showing the performance with 800 (1%) bounding box annotations. Under the same initialization conditions, our average performance surpasses the SOAT by 2.23%, especially improving by 4.17% in the imbalanced class (Cyclist). For the Waymo Dataset, in Fig. B.1(a-b), the Level-1 and Level-2 performance are reported, respectively. Compared to KECOR and CRB, DDFH improves APH by 1.8% and 3.8%, respectively,


doi:10.6342/NTU202401627

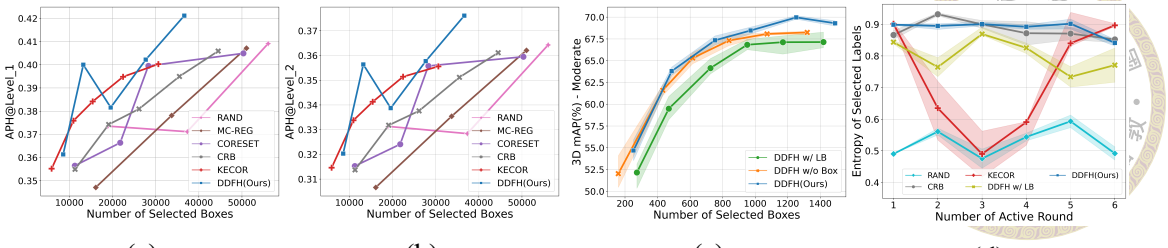


(a) (b) (c) (d)

Figure 4.2: (a-b) report 3D APH of various AL methods on different difficulties in the Waymo dataset. (c) demonstrates the impact on performance when DDFH omits geometric features and replaces confidence balance with label balance. (d) calculates the entropy of the number of samples selected for each class to compare the effectiveness of different AL methods in balancing annotation costs.

Table 4.2: Compare the impact of each component on 3D mAP scores of KITTI dataset at the moderate difficulty

| DD | FH | CB | LB | Average | Car | Pedes. | Cyclist |
|---|---|---|---|---|---|---|---|
| - | - | - | - | 62.97 | 79.44 | 48.93 | 60.52 |
| - | - | - | ✓ | 66.87 | 78.89 | 56.36 | 65.38 |
| - | - | ✓ | - | 67.69 | 78.41 | 54.96 | **69.71** |
| - | ✓ | ✓ | - | 64.73 | 80.15 | 51.09 | 62.94 |
| ✓ | - | ✓ | - | 68.94 | 79.94 | 58.22 | 68.66 |
| ✓ | ✓ | ✓ | - | **69.84** | **80.65** | **59.40** | 69.47 |

and reduces the annotation cost by 56.3% and 66.4%, respectively, demonstrating the effectiveness of DDFH in more diverse and complex scenarios.

### 4.2.2 DDFH with One-Stage Detection Model.

Table 4.1 reports the BEV and 3D mAP scores with 1% annotation bounding boxes. Compared to the SOTA, it improves by approximately 2.8% in 3D mAP and 2.28% in BEV mAP. In Fig. 4.1, we further report the performance growth trend for each category in different levels of difficulty in MOD. DDFH, especially in the car category, which often leads to excessive annotations, can quickly improve performance with the most streamlined annotation cost. For the pedestrian category, the uncertainty-based method performs exceptionally well with a small number of annotations. However, the lack of consideration for diversity limits the performance.


doi:10.6342/NTU202401627

## 4.3 Ablation Study

### 4.3.1 Efficacy of Confidence Balance.

As shown in Table 4.2, CB effectively improves the 3D mAP of the imbalanced class (Cyclist) by 4.3% compared to LB. From Fig. B.1c, it is evident that the performance using LB decreases by an average of 2.8% 3D mAP in each round. In Fig. B.1d, we further demonstrate the label entropy of the selected samples. DDFH can effectively allocate annotation resources in each round, while KECOR sacrifices balance while considering informativeness.

### 4.3.2 Efficacy of Distribution Discrepancy and Feature Heterogeneity.

The results in Table 4.2 show that DD can significantly enhance overall performance, especially in categories with fewer instances, such as pedestrians and cyclists, by focusing more on the selection of these categories due to their larger distribution differences. Using FH alone to estimate informativeness without considering the labeled distribution would be too limiting. The experiments demonstrate that DDFH effectively combines the advantages of both components, resulting in improvements across all categories.

### 4.3.3 Efficacy of Geometric Features.

In Fig. B.1c, the results show that after considering geometric features, DDFH improves the average performance by 1.6% in 3D mAP, confirming that diverse geometric features help the model capture a wider variety of objects.



doi:10.6342/NTU202401627



doi:10.6342/NTU202401627

# Chapter 5 Conclusion

We propose a novel active learning framework DDFH for LiDAR-based 3D object detection that integrates model features with geometric characteristics. By exploring point cloud data through instance-level distribution discrepancy and frame-level feature heterogeneity, and introducing confidence balance, we enhance annotations for imbalanced classes. Our extensive experiments show that compared to SOTA, DDHF reduces annotation costs by 56%, improves performance by 1.8%, and efficiently extracts richer information, demonstrating its effectiveness over current methods.



doi:10.6342/NTU202401627



doi:10.6342/NTU202401627

# References


[1] S. Agarwal, H. Arora, S. Anand, and C. Arora. Contextual diversity for active learning. In Computer Vision–ECCV 2020: 16th European Conference, Glasgow, UK, August 23–28, 2020, Proceedings, Part XVI 16, pages 137–153. Springer, 2020.

[2] J. Ash, S. Goel, A. Krishnamurthy, and S. Kakade. Gone fishing: Neural active learning with fisher embeddings. Advances in Neural Information Processing Systems, 34:8927–8939, 2021.

[3] J. T. Ash, C. Zhang, A. Krishnamurthy, J. Langford, and A. Agarwal. Deep batch active learning by diverse, uncertain gradient lower bounds. In International Conference on Learning Representations, 2020.

[4] A. Athar, E. Li, S. Casas, and R. Urtasun. 4d-former: Multimodal 4d panoptic segmentation. In Conference on Robot Learning, pages 2151–2164. PMLR, 2023.

[5] W. H. Beluch, T. Genewein, A. Nürnberger, and J. M. Köhler. The power of ensembles for active learning in image classification. In Proceedings of the IEEE conference on computer vision and pattern recognition, pages 9368–9377, 2018.

[6] J. W. Cho, D.-J. Kim, Y. Jung, and I. S. Kweon. Mcdal: Maximum classifier discrepancy for active learning. IEEE transactions on neural networks and learning systems, 2022.




doi:10.6342/NTU202401627

[7] J. Choi, I. Elezi, H.-J. Lee, C. Farabet, and J. M. Alvarez. Active learning for deep object detection via probabilistic modeling. In Proceedings of the IEEE/CVF International Conference on Computer Vision, pages 10264–10273, 2021.

[8] L. E. Dor, A. Halfon, A. Gera, E. Shnarch, L. Dankin, L. Choshen, M. Danilevsky, R. Aharonov, Y. Katz, and N. Slonim. Active learning for bert: an empirical study. In Proceedings of the 2020 conference on empirical methods in natural language processing (EMNLP), pages 7949–7962, 2020.

[9] D. Feng, X. Wei, L. Rosenbaum, A. Maki, and K. Dietmayer. Deep active learning for efficient training of a lidar 3d object detector. In 2019 IEEE Intelligent Vehicles Symposium (IV), pages 667–674. IEEE, 2019.

[10] Y. Gal, R. Islam, and Z. Ghahramani. Deep bayesian active learning with image data. In International conference on machine learning, pages 1183–1192. PMLR, 2017.

[11] A. Geiger, P. Lenz, and R. Urtasun. Are we ready for autonomous driving? the kitti vision benchmark suite. In 2012 IEEE conference on computer vision and pattern recognition, pages 3354–3361. IEEE, 2012.

[12] A. Ghita, B. Antoniussen, W. Zimmer, R. Greer, C. Creß, A. Møgelmose, M. M. Trivedi, and A. C. Knoll. Activeanno3d–an active learning framework for multi-modal 3d object detection. arXiv preprint arXiv:2402.03235, 2024.

[13] A. Harakeh, M. Smart, and S. L. Waslander. Bayesod: A bayesian approach for uncertainty estimation in deep object detectors. In 2020 IEEE International Conference on Robotics and Automation (ICRA), pages 87–93. IEEE, 2020.

[14] A. J. Joshi, F. Porikli, and N. Papanikolopoulos. Multi-class active learning for image



doi:10.6342/NTU202401627

classification. In 2009 ieee conference on computer vision and pattern recognition, pages 2372–2379. IEEE, 2009.

[15] C.-C. Kao, T.-Y. Lee, P. Sen, and M.-Y. Liu. Localization-aware active learning for object detection. In Computer Vision–ACCV 2018: 14th Asian Conference on Computer Vision, Perth, Australia, December 2–6, 2018, Revised Selected Papers, Part VI 14, pages 506–522. Springer, 2019.

[16] Y. Luo, Z. Chen, Z. Fang, Z. Zhang, M. Baktashmotlagh, and Z. Huang. Kecor: Kernel coding rate maximization for active 3d object detection. In Proceedings of the IEEE/CVF International Conference on Computer Vision, pages 18279–18290, 2023.

[17] Y. Luo, Z. Chen, Z. Wang, X. Yu, Z. Huang, and M. Baktashmotlagh. Exploring active 3d object detection from a generalization perspective. In The Eleventh International Conference on Learning Representations, 2023.

[18] J. Mao, Y. Xue, M. Niu, H. Bai, J. Feng, X. Liang, H. Xu, and C. Xu. Voxel transformer for 3d object detection. In Proceedings of the IEEE/CVF international conference on computer vision, pages 3164–3173, 2021.

[19] D. Maturana and S. Scherer. Voxnet: A 3d convolutional neural network for real-time object recognition. In 2015 IEEE/RSJ international conference on intelligent robots and systems (IROS), pages 922–928. IEEE, 2015.

[20] V. Nath, D. Yang, B. A. Landman, D. Xu, and H. R. Roth. Diminishing uncertainty within the training pool: Active learning for medical image segmentation. IEEE Transactions on Medical Imaging, 40(10):2534–2547, 2020.



doi:10.6342/NTU202401627

[21] Y. Park, W. Choi, S. Kim, D.-J. Han, and J. Moon. Active learning for object detection with evidential deep learning and hierarchical uncertainty aggregation. In The Eleventh International Conference on Learning Representations, 2022.

[22] Y. Park, J. Park, D.-J. Han, W. Choi, H. Kousar, and J. Moon. Distribution aware active learning via gaussian mixtures. 2023.

[23] A. Parvaneh, E. Abbasnejad, D. Teney, G. R. Haffari, A. Van Den Hengel, and J. Q. Shi. Active learning by feature mixing. In Proceedings of the IEEE/CVF conference on computer vision and pattern recognition, pages 12237–12246, 2022.

[24] C. R. Qi, H. Su, K. Mo, and L. J. Guibas. Pointnet: Deep learning on point sets for 3d classification and segmentation. In Proceedings of the IEEE conference on computer vision and pattern recognition, pages 652–660, 2017.

[25] C. R. Qi, L. Yi, H. Su, and L. J. Guibas. Pointnet++: Deep hierarchical feature learning on point sets in a metric space. Advances in neural information processing systems, 30, 2017.

[26] L. Qing, T. Wang, D. Lin, and J. Pang. Dort: Modeling dynamic objects in recurrent for multi-camera 3d object detection and tracking. In Conference on Robot Learning, pages 3749–3765. PMLR, 2023.

[27] S. Roy, A. Unmesh, and V. P. Namboodiri. Deep active learning for object detection. In BMVC, volume 362, page 91, 2018.

[28] S. Schmidt, Q. Rao, J. Tatsch, and A. Knoll. Advanced active learning strategies for object detection. In 2020 IEEE intelligent vehicles symposium (IV), pages 871–876. IEEE, 2020.



doi:10.6342/NTU202401627

[29] D. W. Scott. Multivariate Density Estimation: Theory, Practice, and Visualization. Wiley, aug 1992.

[30] O. Sener and S. Savarese. Active learning for convolutional neural networks: A core-set approach. In International Conference on Learning Representations, 2018.

[31] B. Settles. Active learning literature survey. 2009.

[32] S. Shi, C. Guo, L. Jiang, Z. Wang, J. Shi, X. Wang, and H. Li. Pv-rcnn: Point-voxel feature set abstraction for 3d object detection. In Proceedings of the IEEE/CVF conference on computer vision and pattern recognition, pages 10529–10538, 2020.

[33] S. Shi, L. Jiang, J. Deng, Z. Wang, C. Guo, J. Shi, X. Wang, and H. Li. Pv-rcnn++: Point-voxel feature set abstraction with local vector representation for 3d object detection. International Journal of Computer Vision, 131(2):531–551, 2023.

[34] Y. Siddiqui, J. Valentin, and M. Nießner. Viewal: Active learning with viewpoint entropy for semantic segmentation. In Proceedings of the IEEE/CVF conference on computer vision and pattern recognition, pages 9433–9443, 2020.

[35] B. W. Silverman. Density estimation for statistics and data analysis. 1986.

[36] P. Singhal, R. Walambe, S. Ramanna, and K. Kotecha. Domain adaptation: challenges, methods, datasets, and applications. IEEE access, 11:6973–7020, 2023.

[37] P. Sun, H. Kretzschmar, X. Dotiwalla, A. Chouard, V. Patnaik, P. Tsui, J. Guo, Y. Zhou, Y. Chai, B. Caine, et al. Scalability in perception for autonomous driving: Waymo open dataset. In Proceedings of the IEEE/CVF conference on computer vision and pattern recognition, pages 2446–2454, 2020.



doi:10.6342/NTU202401627

[38] A. Tanwani. Dirl: Domain-invariant representation learning for sim-to-real transfer. In Conference on Robot Learning, pages 1558–1571. PMLR, 2021.

[39] L. Van der Maaten and G. Hinton. Visualizing data using t-sne. Journal of machine learning research, 9(11), 2008.

[40] C. Wang, C. Ma, M. Zhu, and X. Yang. Pointaugmenting: Cross-modal augmentation for 3d object detection. In Proceedings of the IEEE/CVF Conference on Computer Vision and Pattern Recognition, pages 11794–11803, 2021.

[41] D. Wang and Y. Shang. A new active labeling method for deep learning. In 2014 International joint conference on neural networks (IJCNN), pages 112–119. IEEE, 2014.

[42] J. Wu, J. Chen, and D. Huang. Entropy-based active learning for object detection with progressive diversity constraint. In Proceedings of the IEEE/CVF Conference on Computer Vision and Pattern Recognition, pages 9397–9406, 2022.

[43] Y. Yan, Y. Mao, and B. Li. Second: Sparsely embedded convolutional detection. Sensors, 18(10):3337, 2018.

[44] A. J. Yang, S. Casas, N. Dvornik, S. Segal, Y. Xiong, J. S. K. Hu, C. Fang, and R. Urtasun. Labelformer: Object trajectory refinement for offboard perception from lidar point clouds. In Conference on Robot Learning, pages 3364–3383. PMLR, 2023.

[45] Yang, Chenhongyi and Huang, Lichao and Crowley, Elliot J. Plug and Play Active Learning for Object Detection. In Proceedings of the IEEE/CVF Conference on Computer Vision and Pattern Recognition (CVPR), 2024.



doi:10.6342/NTU202401627

[46] D. Yoo and I. S. Kweon. Learning loss for active learning. In Proceedings of the IEEE/CVF conference on computer vision and pattern recognition, pages 93–102, 2019.

[47] T. Yuan, F. Wan, M. Fu, J. Liu, S. Xu, X. Ji, and Q. Ye. Multiple instance active learning for object detection. In Proceedings of the IEEE/CVF Conference on Computer Vision and Pattern Recognition, pages 5330–5339, 2021.



doi:10.6342/NTU202401627



doi:10.6342/NTU202401627

# Appendix A — More Implementation Details

## A.1 More Implementation Details

To ensure the fairness and reproducibility of our experiments, we implemented DDFH and reproduced most of the baselines based on the public ACTIVE-3D-DET toolbox. We followed all KECOR training settings, using Adam as the optimizer, and a onecycle learning scheduler with an initial learning rate of 0.01. The batch size was set to 6, and each active round was trained for 40 epochs before proceeding to a new sampling round. We used one NVIDIA RTX A6000 to complete all experiments. The runtime for an experiment on KITTI and Waymo is approximately 5 and 81 GPU hours, respectively. The model embeddings $f^e$ used in our method are extracted from the second convolutional layer in the shared block of PV-RCNN.



doi:10.6342/NTU202401627



doi:10.6342/NTU202401627

# Appendix B — More Experimental Details

Table B.1: Compare 3D mAP(%) scores for different SOTA apporch in KITTI Dataset when acquiring approximately 1% queried bounding boxes. † indicates the reported performance of the backbone trained with the 100% labeled set.

| | AVERAGE | | | CAR | | | PEDESTRIAN | | | CYCLIST | | |
|---|---|---|---|---|---|---|---|---|---|---|---|---|
| Method | Easy | Mod. | Hard | Easy | Mod. | Hard | Easy | Mod. | Hard | Easy | Mod. | Hard |
| CRB [17] | 79.06 | 66.49 | 61.76 | 90.81 | 79.06 | 74.73 | 62.09 | 54.56 | 48.89 | 84.28 | 65.85 | 61.66 |
| CRB(offi.) | 80.70 | 67.81 | 62.81 | 90.98 | 79.02 | 74.04 | 64.17 | 50.82 | 50.82 | 86.96 | 67.45 | 63.56 |
| KECOR [16] | 79.81 | 67.83 | 62.52 | 91.43 | 79.63 | 74.41 | 63.49 | 56.31 | 50.20 | 84.51 | 67.54 | 62.96 |
| KECOR(offi.) | 81.63 | 68.67 | 63.42 | 91.71 | 79.56 | 74.05 | 65.37 | 57.33 | 51.56 | 87.80 | 69.13 | 64.65 |
| DDFH(Ours) | **82.27** | **69.84** | **64.76** | **91.76** | **80.65** | **76.46** | **66.37** | **59.40** | **52.97** | **88.68** | **69.47** | **64.85** |
| PV-RCNN† | 81.75 | 70.99 | 67.06 | 92.56 | 84.36 | 82.48 | 64.26 | 56.67 | 51.91 | 88.88 | 71.95 | 66.78 |

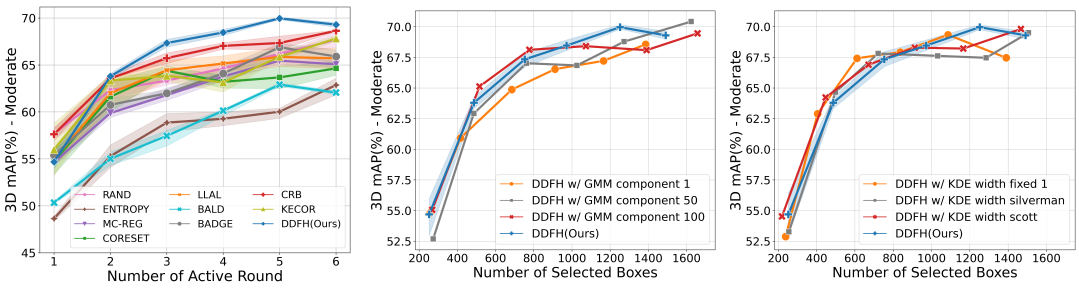


(a) (b) (c)

Figure B.1: (a) report 3D mAP of various AL methods on KITTI in each active round. (b-c) represents the impact of different density estimation methods and varying parameter settings on the performance of DDFH.



doi:10.6342/NTU202401627

## B.1 DDFH in the KITTI Dataset.

In Fig. B.1a, we present the performance of various AL methods in each active round. The number of point clouds in each active round is fixed, allowing us to compare the performance of models under conditions where they have seen the same number of scenes. Notably, KECOR's performance is below expectations given the same number of frames, indicating that KECOR does not effectively consider the diversity information of the scenes. In contrast, DDFH considers frame-level information to avoid redundant instances in similar scenes. The results show that DDFH has a significant advantage in each active round. We present more comprehensive experimental results of DDFH on the KITTI Dataset in Fig. B.2 and Fig. B.3. The results in Fig. B.2 indicate that DDFH with PV-RCNN has a significant advantage in all categories in KITTI, consistent with the results of Figure 4 in main text on SECOND. It is noteworthy that in the car category, some uncertainty-based methods achieve similar performance to DDFH with the same annotation cost. However, these methods fail to improve effectively in other categories, demonstrating DDFH's effectiveness in resource allocation and diversity. Fig. B.3 also provides the trend of average 3D mAP for the one-stage model SECOND in different difficulties, consistent with PV-RCNN, outperforming SOTA methods in all difficulties. Further, in Table B.1, we provide the performance of PV-RCNN trained on 100% labeled data, showing that DDFH's performance with only 1% of bounding box annotation is close to fully trained performance, even outperforming fully trained models in the pedestrian category.



doi:10.6342/NTU202401627

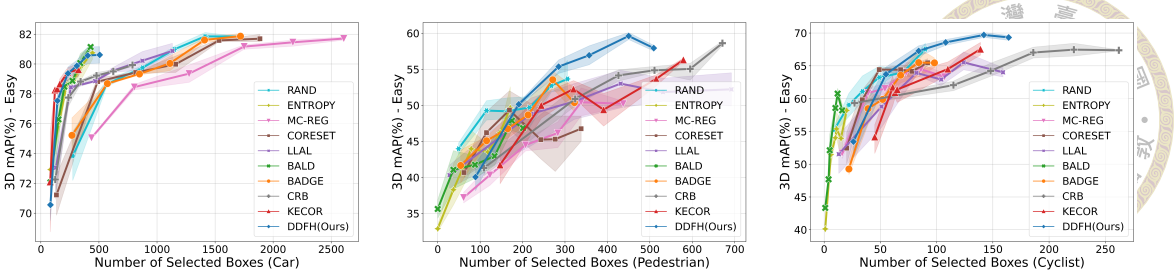


Figure B.2: 3D mAP(%) of DDFH and the AL Baseline across various categories on the KITTI dataset at the moderate difficulty with PV-RCNN.

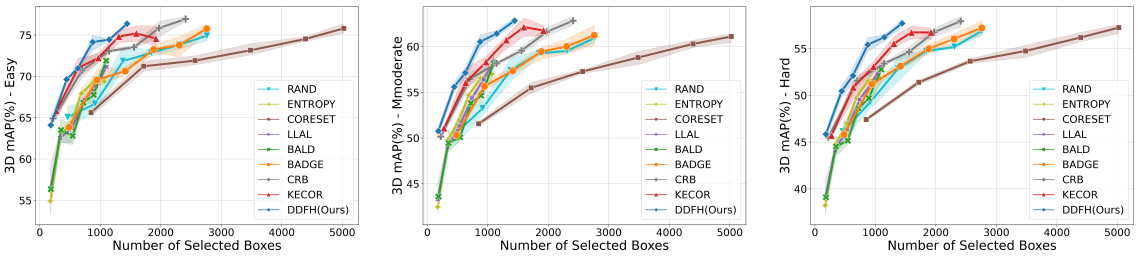


Figure B.3: 3D mAP(%) of DDFH and AL baselines on the KITTI val split with SECOND.

## B.2 Ablation Study of Density Estimation.

We also test the stability and generalizability of DDFH through different density estimation methods and parameters. In Fig. B.1b, we set different numbers of GMM components, specifically 1, 10 (DDFH Ours), 50, and 100. The results indicate that all experiments, except for 1 component, maintain similar effectiveness. In Fig. B.1c, we use Kernel Density Estimation (KDE) to estimate the probability density and adjust different bandwidths to test the stability and generalizability of the DDFH. Silverman [35] and Scott [29] calculate bandwidth based on sample size. The results show that the performance of DDFH remains consistent and stable under different density estimation models and parameters. This is due to the distribution discrepancy focusing on distribution differences and novelty, rather than relying on highly accurate distribution estimates, thus providing sufficient robustness to noisy instances and estimation deviations.


doi:10.6342/NTU202401627



doi:10.6342/NTU202401627

# Appendix C — Limitation

## C.1 Limitation

Considering that the distribution of objects in real environments is often uneven, common objects tend to occupy the majority (e.g. cars). This leads to the underestimation of less frequent categories when estimating informativeness. Therefore, the components DD, FH, and CB in DDFH reduce the impact of uneven distribution at different levels, decrease redundant annotations, and effectively balance minority categories. Although most real-world scenarios exhibit an uneven long-tail distribution, if specific situations lead to a dataset where object distribution is close to a uniform distribution, the effectiveness of DDFH might be limited due to the less apparent distribution differences. A possible solution is to incorporate indicators of uncertainty into DDFH, such as model instability, entropy, or the kernel coding rate combined with KECOR. This approach could address the mentioned limitation and is left for future research.



doi:10.6342/NTU202401627